Matter-wave solitons in an array of spin-orbit-coupled Bose-Einstein condensates

Yanchao Zhang,[1] Chao Hang,[1,2,3,*] and Guoxiang Huang[1,2,3]

[1]*State Key Laboratory of Precision Spectroscopy, East China Normal University, Shanghai 200241, China*
[2]*NYU-ECNU Institute of Physics, New York University at Shanghai, Shanghai 200062, China*
[3]*Collaborative Innovation Center of Extreme Optics, Shanxi University, Taiyuan, Shanxi 030006, China*

(Received 23 April 2023; accepted 29 June 2023; published 28 July 2023)

We investigate matter-wave solitons in a binary Bose-Einstein condensate (BEC) with spin-orbit (SO) coupling, loaded in a one-dimensional (1D) deep optical lattice and a three-dimensional anisotropic magnetic trap, which creates an array of elongated sub-BECs with transverse tunneling. We show that the system supports 1D continuous and discrete solitons localized in the longitudinal (along the array) and the transverse (across the array) directions, respectively. In addition, such solitons are always unpolarized in the zero-momentum state but polarized in finite-momentum states. We also show that the system supports stable two-dimensional semidiscrete solitons, including single- and multiple-peaked ones, localized in both the longitudinal and transverse directions. Stability diagrams for single-peaked semidiscrete solitons in different parameter spaces are identified. The results reported here are beneficial not only for understanding the physical property of SO-coupled BECs but also for generating new types of matter-wave solitons.

DOI: 10.1103/PhysRevE.108.014208

I. INTRODUCTION

Spin-orbit (SO) coupling describes an interaction occurring between internal spin and external orbit motions of a microscopic particle [1]. It can be regarded as the contribution of an effective magnetic field seen by the spin in the frame where the particle is at rest. The first and best-known effect induced by SO coupling is the splitting of spectral lines of atomic energy levels. Due to a relation between angular momentum and nuclear force, a similar effect occurs for protons and neutrons moving inside an atomic nucleus, leading to the energy-level shifts of the nucleus. SO coupling plays also an important role in solid-state physics, the study of which has stimulated many interesting findings, including topological insulators [2,3] and the spin Hall effect [4,5], are promising for many applications (including the design of novel spin devices) [6,7].

In recent years, tremendous efforts have been paid to the research on the generation and engineering of synthetic gauge fields and SO coupling in cold atomic gases [8–15]. Based on the tunability of the SO coupling realized in atomic gases, one can not only investigate many phenomena in solid-state physics in a controllable and disorder-free way, but also reach parameter regimes not easy to access with conventional solid-state materials, and hence allow us to explore more exotic matter states [16–22]. For example, for a homogeneous SO-coupled atomic Bose-Einstein condensate (BEC), its ground state can display a stripe phase, i.e., the atomic gas has a periodic density distribution and hence continuous translation symmetry of the system is broken [23–28]. Moreover, Zitterbewegung oscillations have been found for the center-of-mass motion of SO-coupled BECs [29,30]. In addition, roton-maxon structures, roton softening, and relevant phonon modes in the spectra of SO-coupled BEC s have also been observed [31–33].

Bose-condensed atomic gases have unique features and the interplay between SO coupling and these features can lead to many intriguing new phenomena [34,35]. Particularly, the interplay of SO coupling and atom-atom interactions can give rise to various self-localized states, such as solitons and vortices [36–54]. Furthermore, when a SO-coupled BEC is loaded in an optical lattice, the lattice effect can open energy gaps, resulting in the formation of gap solitons [55–59]. Such solitons exhibit interesting features that are absent in the BEC without SO coupling (e.g., the violation of Galilean invariance) [60,61]. Additionally, the SO coupling can also be used to stabilize high-dimensional solitons in BECs [40–48]. Particularly, when the optical lattices are deep enough, the SO-coupled BECs are localized only at each lattice potential minimum, splitting into sub-BECs, and hence the gap solitons and nonlinear modes created in BECs become discrete [62–64].

In this article, we consider a binary BEC with a SO coupling, loaded in a one-dimensional (1D) deep optical lattice and a highly anisotropic three-dimensional (3D) magnetic trap, which creates an array of quasi-1D condensates with transverse tunneling. The SO coupling is assumed to be generated via a Raman coupling of two atomic hyperfine states. We show that the system supports 1D continuous solitons localized in the longitudinal (along the array) direction, and 1D discrete solitons localized in the transverse (across the array) direction. We find that such solitons are always unpolarized (the densities of two spin-components are equal) in zero-momentum state but are polarized (the densities of two spin-components are unequal) in finite-momentum states.

Furthermore, we demonstrate that the system supports the existence of stable two-dimensional (2D) matter-wave

*chang@phy.ecnu.edu.cn

solitons, which are localized in both longitudinal and transverse directions and can exhibit single- and multi-peaked density distributions. Such solitons can be taken as semidiscrete solitons, since they have continuous and discrete density distributions in the longitudinal and transverse directions, respectively. We also consider the stability of such solitons, and identify their stability diagram in different parameter regions.

Before proceeding, we would like to stress that, although in the past years many studies on matter-wave solitons in binary BECs with SO coupling have been reported, our work is distinct from them based on the following reasons:

(i) In previous studies [40–48], high-D solitons were obtained in free space. The stabilization of solitons is realized through Rashba SO coupling, by which the solitons have forms of semivortices or vortex mixed modes [41–43,48]; another way for soliton stabilization is to employ dipole-dipole interaction between atoms, which needs the use of dipolar BECs with SO coupling [44–46]. Differently, in our work the SO coupling is realized via the Raman coupling of atomic hyperfine states, which is equivalent to an equal-weight superposition of Rashba and Dresselhaus SO couplings [65] and can be easily realized in experiments. The atom-atom interaction in the BEC is a local one and hence our model can be realized by using a conventional BEC. The stabilization of the solitons can be achieved by the joint contribution of the SO coupling and the trapping potential (i.e., 1D optical lattice and a 3D magnetic trap).

(ii) Gap solitons in a SO-coupled BEC with a shallow optical lattice potential were considered in Refs. [55–59], where the system was modeled by a continuous nonlinear Schrödinger (NLS) equation with a periodic potential, allowing gap solitons which are bifurcated from the band edge of linear Bloch modes. At variance with such a consideration, in our work a 1D deep optical lattice is used and thus the BEC is split into an array of quasi-1D sub-BECs with transverse tunneling; the system is modeled by a discrete NLS equation, in which the underlying periodicity and discreteness leads to new families of matter-wave solitons that have no counterpart in continuous models. The atomic density for such solitons distributes only in very few lattice sites, much more localized in space than the gap solitons obtained in Refs. [55–59].

(iii) The system proposed in our study can support various matter-wave solitons (including 1D continuous solitons localized in the longitudinal direction, 1D discrete solitons localized in the transverse direction, and 2D semidiscrete solitons localized in both the longitudinal and the transverse directions), which are not easy to realize in other settings. Thereby, such a system may be regarded as an effective platform for the study of novel nonlinear matter waves based on SO-couplings. The research results reported here are useful not only for understanding the unique property of SO-coupled BECs, but also for finding new types of matter-wave solitons in Bose-condensed atomic gases.

The remainder of the article is organized as follows: In Sec. II, we describe the physical model under study; the linear dispersion relation of the system is discussed. In Sec. III, we investigate the formation and propagation of 1D continuous and discrete solitons; the polarization of the solitons is analyzed. In Sec. IV, we investigate the 2D single- and multi-peaked semidiscrete solitons, and give the stability diagram of the semidiscrete solitons in different parameter regions. Finally, in the last section we give a summary of the main results obtained in the present study.

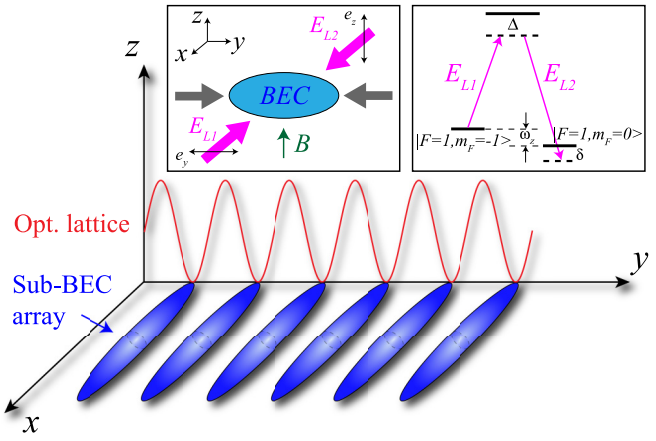

FIG. 1. Physical model under study. The red curve denotes the optical lattice and the blue ellipsoids denote the array of sub-BECs. The geometrical configuration of the setting and the level diagram are shown in the left and right insets, respectively. The SO coupling is generated by two Raman laser fields E_{L1} and E_{L2} (magenta arrows along x direction), which have orthogonal linear polarizations $\mathbf{e}_y$ and $\mathbf{e}_z$ (black double arrows along the y and z directions, respectively). Intermediating by the upper level, E_{L1} and E_{L2} couple the two lower (Zeeman) levels $|F=1, m_F=0\rangle$ and $|F=1, m_F=-1\rangle$ of a Bose-condensed ^{87}Rb atomic gas, which differ in energy by a Zeeman splitting ω_Z caused by the magnetic field B applied along the z direction (denoted by green arrow). E_{L1} and E_{L2} have frequency difference $\omega_Z+\delta$, where δ is a small detuning from the two-photon Raman resonance. Δ is a large (one-photon) detuning.

II. PHYSICAL MODEL AND SMALL-AMPLITUDE SOLUTIONS

A. Physical model

We start with considering an atomic BEC (e.g., a Bose-condensed ^{87}Rb atomic gas) formed in the $F=1$ hyperfine ground-state manifold, which is loaded in a deep, 1D optical lattice and a highly anisotropic 3D magnetic trap; see Fig. 1. We assume that a static magnetic field B is applied along z direction, leading to a Zeeman splitting of the $F=1$ hyperfine ground state, i.e., $F=1$ level is split into three Zeeman sublevels $|F=1, m_F=-1\rangle$, $|F=1, m_F=0\rangle$, and $|F=1, m_F=1\rangle$. The BEC is then coupled to the electric field of two Raman laser fields $\mathbf{E}_{L1}$ and $\mathbf{E}_{L2}$, which have orthogonal linear polarizations $\mathbf{e}_y$ and $\mathbf{e}_z$ (represented by the black double arrows along the y and z directions in the left inset of Fig. 1), wave vectors $\mathbf{k}_{L1}$ and $\mathbf{k}_{L2}$, and angular frequencies ω_{L1} and ω_{L2}, respectively. The frequency splitting between the two Zeeman sublevels $|F=1, m_F=0\rangle$ and $|F=1, m_F=-1\rangle$ (i.e., ω_Z) is set to be close to the frequency difference between the two Raman laser fields (i.e., $\Delta\omega_L=\omega_{L1}-\omega_{L2}$), giving rise to a small two-photon detuning $\delta=\Delta\omega_L-\omega_Z$. The state $|F=1, m_F=1\rangle$ (not shown) is far detuned from the other states and hence can be neglected. Through the coupling of the two Raman laser fields (which are assumed to be undepleted) and intermediation of the upper level, the

system can be regarded as a pseudo-spin-1/2 system, with the two spin components given by $|\uparrow\rangle = |F = 1, m_F = 0\rangle$ and $|\downarrow\rangle = |F = 1, m_F = -1\rangle$. We further assume that the two Raman laser fields counterpropagate along the x direction with approximately equal wave number, i.e., $\mathbf{k}_{L1} \approx -\mathbf{k}_{L2} = \mathbf{e}_x k_L$.

Under the mean-field approximation the Hamiltonian of the system is given by

$$H = \int d^3r \Psi^\dagger(\mathbf{r})[H_{\rm sp} + G]\Psi(\mathbf{r}), \tag{1}$$

where $\mathbf{r} = (x, y, z)$, $d^3r = dxdydz$, $\Psi = (\Psi_\uparrow, \Psi_\downarrow)^T$ is the binary condensate wave function (here $\Psi_\uparrow$ and $\Psi_\downarrow$ are the spin-up and spin-down components, respectively; T means transpose), G is a 2×2 matrix defined by

$$G = 4\pi\hbar N \begin{pmatrix} a_{\uparrow\uparrow}|\Psi_\uparrow|^2 + a_{\uparrow\downarrow}|\Psi_\downarrow|^2 & 0 \\ 0 & a_{\downarrow\uparrow}|\Psi_\uparrow|^2 + a_{\downarrow\downarrow}|\Psi_\downarrow|^2) \end{pmatrix}, \tag{2}$$

characterizing the atom-atom interaction, with N the number of atoms and $a_{\alpha\beta}$ ($\alpha, \beta = \uparrow, \downarrow$) the s-wave scattering lengths for the same ($a_{\uparrow\uparrow}$, $a_{\downarrow\downarrow}$) and different ($a_{\uparrow\downarrow}$ and $a_{\downarrow\uparrow}$) spin-components.

In the expression (1), $H_{\rm sp}$ is single-particle Hamiltonian with the form

$$H_{\rm sp} = -\frac{\hbar^2}{2M}\nabla^2 - i\frac{\hbar^2 k_L}{M}\frac{\partial}{\partial x}\sigma_z + \hbar\Omega\sigma_x + V(\mathbf{r}), \tag{3}$$

where $\nabla = (\partial_x, \partial_y, \partial_z)$, M is atomic mass, σ_x and σ_z are Pauli matrices, and $\Omega = |\Omega_L|^2/\Delta$ describes the Raman coupling (Ω_L is the half Rabi frequency of each Raman laser field and Δ is a one-photon frequency detuning), which is assumed large for suppressing the spontaneous emission from the upper level. Since Ω is proportional to the Raman laser intensity $|\Omega_L|^2$ and inversely proportional to the detuning Δ, it can be easily tuned experimentally. The term $-i(\hbar^2 k_L/M)\partial_x\sigma_z$ in the expression (3) is the contribution from the Raman-induced SO coupling, which describes the momentum exchange between the atom and the Raman laser fields, as well as the coupling with the atomic spin. The strength of the SO coupling is characterized by the parameter $\hbar^2 k_L/M = 2\pi\hbar^2/(M\lambda_L)$, i.e., inversely proportional to the atomic mass M and the wavelength λ_L of the Raman laser fields.

We assume that the potential $V(\mathbf{r})$ originates from contributions of a 1D optical lattice in the y direction and an anisotropic 3D magnetic trap. It has the form

$$V(\mathbf{r}) = V_0 \sin^2\left(\frac{\pi y}{d}\right) + \frac{M}{2}\left(\omega_x^2 x^2 + \omega_y^2 y^2 + \omega_z^2 z^2\right), \tag{4}$$

where V_0 (d) is the depth (period) of the optical lattice, and ω_α ($\alpha = x, y, z$) are the trapping frequencies in the three directions of the magnetic trap, satisfying the condition of high anisotropy $\omega_x \approx \omega_y \ll \omega_z$. If the optical lattice along the y direction is deep enough, taking into account that the trapping effect of the magnetic trap in the z direction is much larger than that in the other (x and y) directions, the Bose-condensed atomic gas will become an array of quasi-1D subcondensates (see the lower part of Fig. 1). However, the atoms can still tunnel between adjacent lattice sites and, as a result, they are coupled weakly in the y direction.

For the convenience of the following calculations, we introduce the dimensionless variables $(\xi, \eta, \zeta) = a_z^{-1}(x, y, z)$, $\tau = \omega_z t$, and $(\varphi_\uparrow, \varphi_\downarrow) = (\Psi_\uparrow, \Psi_\downarrow)/\sqrt{n_0}$, with $a_z = \sqrt{\hbar/(M\omega_z)}$ the harmonic oscillator length in the y and z directions and $n_0 = N/a_z^3$ the atomic density. Then, from the Hamiltonian (1) we obtain the dimensionless Gross–Pitaevskii (GP) equations for the two spin components:

$$i\frac{\partial\varphi_\uparrow}{\partial\tau} = -\frac{1}{2}\left[\tilde\nabla^2 - \frac{2V_0}{\hbar\omega_z}\sin^2\left(\frac{\pi\eta}{\tilde d}\right) - \zeta^2\right]\varphi_\uparrow - i\tilde k_L\frac{\partial\varphi_\uparrow}{\partial\xi} + \tilde\Omega\varphi_\downarrow + (g_{\uparrow\uparrow}|\varphi_\uparrow|^2 + g_{\uparrow\downarrow}|\varphi_\downarrow|^2)\varphi_\uparrow, \tag{5a}$$

$$i\frac{\partial\varphi_\downarrow}{\partial\tau} = -\frac{1}{2}\left[\tilde\nabla^2 - \frac{2V_0}{\hbar\omega_z}\sin^2\left(\frac{\pi\eta}{\tilde d}\right) - \zeta^2\right]\varphi_\downarrow + i\tilde k_L\frac{\partial\varphi_\downarrow}{\partial\xi} + \tilde\Omega\varphi_\uparrow + (g_{\downarrow\uparrow}|\varphi_\uparrow|^2 + g_{\downarrow\downarrow}|\varphi_\downarrow|^2)\varphi_\downarrow, \tag{5b}$$

with $\tilde\nabla = (\partial_\xi, \partial_\eta, \partial_\zeta)$, $\tilde d = d/a_z$, $\tilde k_L = k_L a_z$, and $\tilde\Omega = \Omega/\omega_z$. Here, $g_{\alpha\beta} = 4\pi N a_{\alpha\beta}/a_z$ ($\alpha, \beta = \uparrow, \downarrow$) characterize the atomic interactions for the same ($g_{\uparrow\uparrow}$ and $g_{\downarrow\downarrow}$) and different ($g_{\uparrow\downarrow}$ and $g_{\downarrow\uparrow}$) spin components. Since $a_{\uparrow\uparrow} \approx a_{\downarrow\downarrow}$ and $a_{\uparrow\downarrow} \approx a_{\downarrow\uparrow}$, we set $g_{\uparrow\uparrow} \approx g_{\downarrow\downarrow} = g_1$ and $g_{\uparrow\downarrow} \approx g_{\downarrow\uparrow} = g_2$. Moreover, for deriving Eqs. (5), we have neglected the terms $-(\omega_x^2/\omega_z^2)\xi^2$ and $-(\omega_y^2/\omega_z^2)\eta^2$, which are very small due to the condition $\omega_z \gg \omega_x, \omega_y$. From Eqs. (5), we see that the condition of the deep optical lattice is given by $V_0/(\hbar\omega_z) \gg \tilde d^2$.

To estimate the magnitude of dimensionless parameters given above, we choose a set of practical parameters with the trapping frequencies $\omega_x \approx \omega_y \approx 2\pi \times 1$ Hz and $\omega_z \approx 2\pi \times 15$ Hz, which leads $a_z \approx 2.8$ μm. Through the use of Feshbach resonance, the s-wave scattering length for ^{85}Rb BECs can be tuned to be negative (corresponding to the attractive atomic interactions), giving by $a_{\alpha\beta} \approx -10.9\, a_0$ ($a_0 = 0.0529$ nm is the Bohr radius) [66,67], and if the total number of condensed atoms $N \approx 10^4$, the atomic density $n_0 \approx 4.7 \times 10^{14}$ cm^{-3} and the atomic interactions $g_1 \approx g_2 \approx -26$. Moreover, we take $k_L \approx 1/a_z \approx 3.6 \times 10^5$ m^{-1} ($\lambda_L \approx 17.5$ μm), $\Omega_L \approx 0.5 \times 10^6$ s^{-1}, and $\Delta \approx 2.6$ GHz, then the strengths of the SO coupling and Raman coupling are of the same order of magnitude of one, i.e., $\tilde k_L \approx \tilde\Omega \approx 1$. Note that both $\tilde k_L$ and $\tilde\Omega$ are tunable by changing ω_z, Ω_L, and Δ in the present system, providing an ideal platform for the study of various solitons (see below). We also choose $V_0 \approx \hbar\omega_z/2$ so that the condition of the deep optical lattice reads $\tilde d^2 \ll 1/2$, which can be safely satisfied by taking $d \ll a_z$.

We are interested in the nonlinear excitations in the system for the case where the BEC is tightly confined in the minima of the optical lattice and the magnetic trap. To this end, we make simplification for the Eqs. (5) under assumptions indicated above. As a first step, we consider the following eigenvalue problems associated with the solutions of Eqs. (5) [see Eqs. (7) and (9) below], given by

$$-\frac{\partial^2\phi_{k,\alpha}(\eta)}{\partial\eta^2} + \frac{2V_0}{\hbar\omega_z}\sin^2\left(\frac{\pi\eta}{\tilde d}\right)\phi_{k,\alpha}(\eta) = \mathcal{E}_\alpha\phi_{k,\alpha}(\eta), \tag{6a}$$

$$-\frac{\partial^2\beta_m(\zeta)}{\partial\zeta^2} + \zeta^2\beta_m(\zeta) = \varepsilon_m\beta_m(\zeta), \tag{6b}$$

where $\phi_{k,\alpha}(\eta)$ are Bloch functions, describing the condensate distribution in the y direction, with α and k being the band

number and Bloch vector in the first Brillouin zone. Since the energy $\mathcal{E}_\alpha$ is periodic in the momentum space, $\mathcal{E}_\alpha(k) = \mathcal{E}_\alpha(k + 2\pi/\tilde{d})$, it can be represented in the form of discrete Fourier series $\mathcal{E}_\alpha(k) = \sum_n \hat{\omega}_{n,\alpha} e^{ikn\tilde{d}}$, with $\hat{\omega}_{n,\alpha} = \hat{\omega}_{-n,\alpha} = \hat{\omega}^*_{n,\alpha}$. Since the functions $\phi_{k,\alpha}(\eta)$ are strongly localized at the lattice minima, it implies $|\int \phi^*_{k,\alpha}(\eta)\phi_{k,\alpha}(\eta - n\tilde{d})d\eta| \approx \delta_{0,n}$, which is analogous to the tight-binding approximation of solid-state physics [68].

Although Bloch functions constitute a complete orthogonal basis, for the deep lattice of the present case it is more convenient to use Wannier functions instead of Bloch functions. We recall that the Wannier functions are centered around the position $\eta = n\tilde{d}$ ($n \in \mathbb{Z}$) and defined as [69]

$$w_{n,\alpha}(\eta) = w_{n,\alpha}(\eta - n\tilde{d}) = \frac{\tilde{d}}{2\pi}\int_{-\pi/\tilde{d}}^{\pi/\tilde{d}} \phi_{k,\alpha}(\eta)e^{-ikn\tilde{d}}dk. \quad (7)$$

The inverse transformation is given by $\phi_{k,\alpha}(\eta) = \sum_n w_{n,\alpha}(\eta)e^{ikn\tilde{d}}$. Wannier functions form a complete orthogonal set of functions with respect to both n and α, which can be made real and exponentially decaying at infinity.

Equation (6b) has the form of the eigenvalue equation of a 1D harmonic oscillator in quantum mechanics [70]. Thus its solution reads

$$\beta_m(\zeta) = \frac{1}{\sqrt{\sqrt{\pi}2^m m!}} H_m(\zeta)e^{-\zeta^2/2}, \quad (8)$$

with eigenvalue $\varepsilon_m = 2(m + 1/2)$, $m = 0, 1, 2, \ldots$. Here $H_m(\zeta)$ are Hermite polynomials, forming a complete and orthogonal set of functions with respect to quantum number m. Particularly, for the lowest state ($m = 0$) one has $\beta_0(\zeta) = \pi^{-1/4}e^{-\zeta^2/2}$, with eigenenergy $\varepsilon_0 = 1$.

Based on the completeness of Wannier functions and the Hermite polynomials given above, any solution of Eqs. (5) can be expanded with the form

$$\varphi_\uparrow(\xi, \eta, \zeta, \tau) = \sum_{j,\alpha,m} w_{j,\alpha}(\eta)\beta_m(\zeta)\psi_{\uparrow,j,\alpha,m}(\xi, \tau), \quad (9a)$$

$$\varphi_\downarrow(\xi, \eta, \zeta, \tau) = \sum_{j,\alpha,m} w_{j,\alpha}(\eta)\beta_m(\zeta)\psi_{\downarrow,j,\alpha,m}(\xi, \tau). \quad (9b)$$

For simplicity, we make the following assumptions: (i) The trapping potential in the z direction is strong enough, so that the excitation of atoms to upper levels ε_m ($m \geqslant 1$) is negligible. Thus one can take $\beta_m(\zeta) \approx \beta_0(\zeta)\delta_{m,0}$. (ii) The optical lattice in the y direction is deep enough, so that only the excitation in the lowest band plays a significant role. Hence one can take $w_{j,\alpha}(\eta) \approx w_{j,1}(\eta)\delta_{\alpha,1}$. As a result, the expressions (9) is reduced into

$$\varphi_\uparrow(\xi, \eta, \zeta, \tau) = \beta_0(\zeta)\sum_j w_j(\eta)\psi_{\uparrow,j}(\xi, \tau), \quad (10a)$$

$$\varphi_\downarrow(\xi, \eta, \zeta, \tau) = \beta_0(\zeta)\sum_j w_j(\eta)\psi_{\downarrow,j}(\xi, \tau), \quad (10b)$$

where we have dropped the band index.

Substituting solutions (10) into Eqs. (5), multiplying $\int_{-\infty}^{\infty} d\eta w_j(\eta)\int_{-\infty}^{\infty} d\zeta \beta_0(\zeta)$, and using the orthogonality of Wannier functions $\int_{-\infty}^{\infty} w_j(\eta)w_{j'}(\eta)d\eta = \delta_{j,j'}$ and the normalization condition $\int_{-\infty}^{\infty} \beta_0^2(\zeta)d\zeta = 1$, we obtain the reduced GP equations

$$\begin{aligned} i\frac{\partial\psi_{\uparrow,j}}{\partial\tau} = & -\frac{1}{2}\frac{\partial^2\psi_{\uparrow,j}}{\partial\xi^2} - i\tilde{k}_L\frac{\partial\psi_{\uparrow,j}}{\partial\xi} - \chi(\psi_{\uparrow,j+1} + \psi_{\uparrow,j-1}) \\ & + \tilde{\Omega}\psi_{\downarrow,j} + (W_1|\psi_{\uparrow,j}|^2 + W_2|\psi_{\downarrow,j}|^2)\psi_{\uparrow,j}, \quad (11a) \end{aligned}$$

$$\begin{aligned} i\frac{\partial\psi_{\downarrow,j}}{\partial\tau} = & -\frac{1}{2}\frac{\partial^2\psi_{\downarrow,j}}{\partial\xi^2} + i\tilde{k}_L\frac{\partial\psi_{\downarrow,j}}{\partial\xi} - \chi(\psi_{\downarrow,j+1} + \psi_{\downarrow,j-1}) \\ & + \tilde{\Omega}\psi_{\uparrow,j} + (W_2|\psi_{\uparrow,j}|^2 + W_1|\psi_{\downarrow,j}|^2)\psi_{\downarrow,j}. \quad (11b) \end{aligned}$$

Here $\tilde{k}_L$ characterizes the strength of the SO coupling, $\chi = -\hat{\omega}_1 = -\hat{\omega}_{-1}$ characterizes the coupling between adjacent lattice sites due to the atomic tunneling, $\tilde{\Omega}$ characterizes the Raman coupling, and $W_1 = (g_1/2)\int w_j^4 d\eta$ [$W_2 = (g_2/2)\int w_j^4 d\eta$] describes the strength of the intracomponent (intercomponent) interaction. Note that, owing to the strong localization of Wannier functions around lattice sites, in Eqs. (11) the contribution by next nearest neighbor lattice sites along the y direction plays a negligible role and hence has been disregarded; furthermore, both W_1 and W_2 can be approximately taken as to be independent of the site number j.

The reduced GP Eqs. (11) are semidiscrete (2 + 1)D equations, describing the nonlinear coupling (due to the mean-field and the SO interactions) between the two spin components. In addition to the independent time variable τ, they have the continuous independent space variable along the x direction (i.e., ξ) and the discrete independent space variable along the y direction (i.e., j).

B. Small-amplitude solutions and linear dispersion relation

For a dilute SO-coupled BEC, the small-amplitude solution of Eqs. (11) can be sought by neglecting the nonlinear effect (i.e., taking $W_1 \approx W_2 \approx 0$). It has the form of a two-component plane-wave solution $(\psi_{\uparrow,j}, \psi_{\downarrow,j})^T = (a, b)^T e^{ik\xi + iqj - i\omega\tau}$. Here, a and b are amplitudes of the two components; k and q are atomic and lattice momentums along the x and y directions, respectively. Substituting such a plane-wave solution into Eqs. (11), we obtain

$$\begin{pmatrix} \frac{k^2}{2} + \tilde{k}_L k - 2\chi\cos q & \tilde{\Omega} \\ \tilde{\Omega} & \frac{k^2}{2} - \tilde{k}_L k - 2\chi\cos q \end{pmatrix}\begin{pmatrix} a \\ b \end{pmatrix} = \omega\begin{pmatrix} a \\ b \end{pmatrix}, \quad (12)$$

which leads to two branches of linear dispersion relation

$$\omega = \omega_\pm \equiv \frac{1}{2}k^2 - 2\chi\cos q \pm \sqrt{\tilde{k}_L^2 k^2 + \tilde{\Omega}^2}. \quad (13)$$

If q is fixed, the upper branch ω_+ always has a minimum at $(k, \omega) = (0, -2\chi\cos q + \tilde{\Omega})$. Differently, the lower branch ω_- has different behavior depending on the sign of the parameter $1 - \tilde{\Omega}/\tilde{k}_L^2$: if $1 - \tilde{\Omega}/\tilde{k}_L^2 \leqslant 0$, it has a minimum at $(k, \omega) = (0, -2\chi\cos q - \tilde{\Omega})$ (Case I); however, if $1 - \tilde{\Omega}/\tilde{k}_L^2 > 0$ it has a maximum at

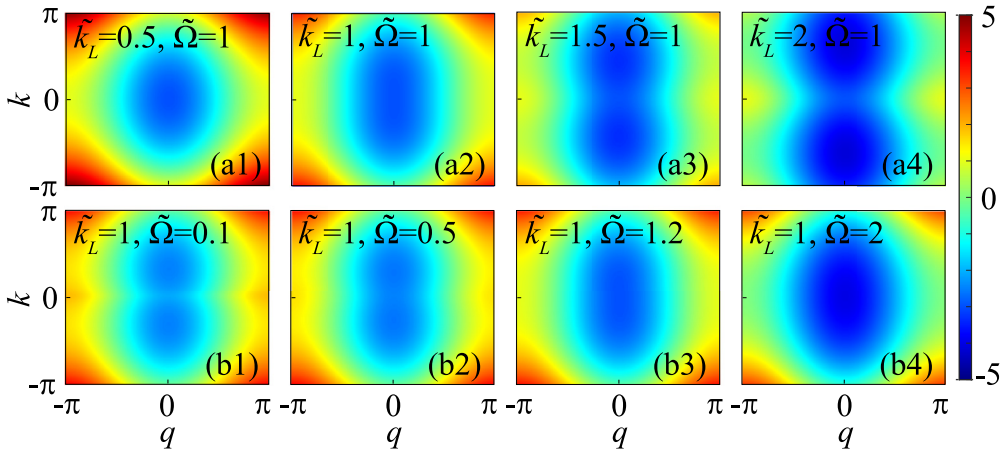

FIG. 2. Linear dispersion relation of the lower branch, i.e., ω_-, as a function of the atomic and lattice momentums k and q for tunneling coefficient $\chi = 1$ and different strengths of the SO coupling $\tilde{k}_L$ and the Raman coupling $\tilde{\Omega}$. Panels (a1), (a2), (a3), and (a4) are for $(\tilde{k}_L, \tilde{\Omega}) =$ (0.5, 1), (1,1), (1.5,1), and (2,1), respectively; panels (b1), (b2), (b3), and (b4) are for $(\tilde{k}_L, \tilde{\Omega}) = (1, 0.1)$, (1,0.5), (1,1.2), and (1,2), respectively.

$(k, \omega) = (0, -\tilde{\Omega})$ and two minima at $(k, \omega) = (\pm k_{\min}, \omega_{\min})$ (Case II), with

$$k_{\min} = \sqrt{\tilde{k}_L^2 - (\tilde{\Omega}/\tilde{k}_L)^2}, \tag{14a}$$

$$\omega_{\min} = -2\chi \cos q - \frac{1}{2}\left[\tilde{k}_L^2 + (\tilde{\Omega}/\tilde{k}_L)^2\right]. \tag{14b}$$

On the other hand, if k is fixed, the upper and lower branches have minima at $(q, \omega) = (0, \frac{1}{2}k^2 - 2\chi \pm (\tilde{k}_L^2 k^2 + \tilde{\Omega}^2)^{1/2})$, respectively.

Shown in Fig. 2 is the distribution of ω_- as a function of the atomic and lattice momentums k and q for the tunneling coefficient $\chi = 1$ and different strengths of the SO coupling $\tilde{k}_L$ and the Raman coupling $\tilde{\Omega}$. Figures 2(a1)–2(a4) in the figure are respectively for $(\tilde{k}_L, \tilde{\Omega}) = (0.5, 1)$, (1,1), (1.5,1), and (2,1) (i.e., varying $\tilde{k}_L$, fixing $\tilde{\Omega}$); Figs. 2(b1)–2(b4) are respectively for $(\tilde{k}_L, \tilde{\Omega}) = (1, 0.1)$, (1,0.5), (1,1.2), and (1,2) (i.e., varying $\tilde{\Omega}$ but fixing $\tilde{k}_L$). We see that there exists a critical value of $\tilde{k}_L$, i.e., $\tilde{k}_L^{\rm cr} = \sqrt{\tilde{\Omega}}$. For $\tilde{k}_L \leqslant \tilde{k}_L^{\rm cr}$, ω_- has a single-well distribution with only one minimum at zero momentum $k = 0$ in the x direction [i.e., Case I, including Figs. 2(a1), 2(a2), 2(b3), and 2(b4)]. However, for $\tilde{k}_L > \tilde{k}_L^{\rm cr}$, ω_- has a double-well distribution with two minima at nonzero momentum $k = \pm k_{\min}$ [i.e., Case II, including Figs. 2(a3), 2(a4), 2(b1), and 2(b2)]. Therefore, by increasing the SO coupling $\tilde{k}_L$ or decreasing the Raman coupling $\tilde{\Omega}$, one can promote the phase transition from a mode with zero momentum to that with finite momentum, or a linear superposition of both modes with finite momentums, which can results in the formation of "stripe phase." On the other hand, in the y direction, ω_- always has only one minimum at $q = 0$.

III. ONE-DIMENSIONAL CONTINUOUS AND DISCRETE MATTER-WAVE SOLITONS

Because the system under consideration possesses interatomic interaction [characterized by the interaction energy related to (2)] and dispersion [characterized by the atomic kinetic energy, i.e., the first term in (3)], it is possible to generate various matter-wave solitons through balancing the dispersion and nonlinear effects and manipulating the optical lattice and SO coupling in the system. In particular, the system allows the existence of 1D continuous solitons localized in the x direction and 1D discrete solitons localized in the y direction, as shown below.

A. One-dimensional continuous matter-wave solitons localized in the x direction

For 1D solitons localized in the x direction (along the condensate array), the array has a marginal effect on the solitons and their properties are mainly determined by the linear dispersion relation of the system. From (13), we see that for $\omega < -2\chi - \tilde{\Omega}$ (Case I) or $\omega < \omega_{\min}$ (Case II), there exists a semi-infinite gap where the linear modes are forbidden to exist. However, gap solitons might be found in such semi-infinite gap analytically or numerically. By using the transformation

$$\begin{pmatrix} \psi_{\uparrow,j}(\xi,\tau) \\ \psi_{\downarrow,j}(\xi,\tau) \end{pmatrix} = \begin{pmatrix} c_{\uparrow,q}(\xi,\tau) \\ c_{\downarrow,q}(\xi,\tau) \end{pmatrix} e^{iqj}, \tag{15}$$

where $-J/2 \leqslant j \leqslant J/2$ with J the total number of lattice sites, based on the reduced GP Eqs. (11), we obtain the equations for $c_{\uparrow,q}$ and $c_{\downarrow,q}$, given by

$$i\frac{\partial c_{\uparrow,q}}{\partial \tau} = -\frac{1}{2}\frac{\partial^2 c_{\uparrow,q}}{\partial \xi^2} - i\tilde{k}_L\frac{\partial c_{\uparrow,q}}{\partial \xi} - 2\chi\cos(q)c_{\uparrow,q} + \tilde{\Omega}c_{\downarrow,q} + (W_1|c_{\uparrow,q}|^2 + W_2|c_{\downarrow,q}|^2)c_{\uparrow,q}, \tag{16a}$$

$$i\frac{\partial c_{\downarrow,q}}{\partial \tau} = -\frac{1}{2}\frac{\partial^2 c_{\downarrow,q}}{\partial \xi^2} + i\tilde{k}_L\frac{\partial c_{\downarrow,q}}{\partial \xi} - 2\chi\cos(q)c_{\downarrow,q} + \tilde{\Omega}c_{\uparrow,q} + (W_2|c_{\uparrow,q}|^2 + W_1|c_{\downarrow,q}|^2)c_{\downarrow,q}. \tag{16b}$$

To solve Eqs. (16), we employ the multiscale expansion [36,50]

$$\begin{pmatrix} c_{\uparrow,q} \\ c_{\downarrow,q} \end{pmatrix} = \sum_{n=1}^{\infty} \epsilon^n \begin{pmatrix} A_n \\ B_n \end{pmatrix} \Theta_n(T, X) e^{i(k\xi - \mu\tau)}. \tag{17}$$

Here ϵ is a small parameter characterizing the typical amplitude on the condensate background, A_n and B_n $(n = 1, 2, \ldots)$

are constants, μ is chemical potential, $\Theta_n(T, X)$ are functions of the slow variables $T = \epsilon^2\tau$ and $X = \epsilon(\xi - v\tau)$ (v is a constant characterizing the group velocity of Θ_n). For convenience, we set $\mu = \omega + \epsilon^2\omega_0$, with ω the energy in the linear limit and $\epsilon^2\omega_0$ a small deviation due to the nonlinear effect. Plugging (17) into Eqs. (16) and comparing the powers of ϵ, one can solve Eqs. (16) order by order.

At the first-order ($n = 1$), we get the linear dispersion relation (13), and also $A_1 = 1$ and

$$B_1 = Q \equiv (\omega_- - k^2/2 - \tilde{k}_L k + 2\chi \cos q)/\tilde{\Omega}. \tag{18}$$

At second-order ($n = 2$), we attain the expression of the group velocity, given by $v = \partial\omega_-/\partial k = k - \tilde{k}_L(Q^2 - 1)/(Q^2 + 1)$. Finally, a scalar nonlinear equation of the envelope function $\Theta(T, X)$ can be obtained at the third-order ($n = 3$):

$$i\frac{\partial\Theta}{\partial T} = -\frac{\Lambda}{2}\frac{\partial^2\Theta}{\partial X^2} + S|\Theta|^2\Theta - \omega_0\Theta. \tag{19}$$

Here $\Lambda = \partial^2\omega_-/\partial k^2 = 1 - \tilde{k}_L^2/(\tilde{k}_L^2 k^2 + \tilde{\Omega}^2)^{1/2} + \tilde{k}_L^4 k^2/(\tilde{k}_L^2 k^2 + \tilde{\Omega}^2)^{3/2}$ and $S = (W_1 + 2W_2Q^2 + W_1Q^4)/(1 + Q^2)$, characterizing the effects of dispersion and nonlinearity, respectively.

The signs of the dispersion and nonlinear terms in Eq. (19) are crucial for determining the types of solitons. If $\Lambda S < 0$ ($\Lambda S > 0$), the system supports bright (dark) solitons. Note that the sign of S depends on W_1 and W_2. In the lower energy band (ω_-) and for $k = 0$ (Case I) and $k = k_{\min}$ (Case II), the group velocity is zero ($v = 0$) and one has always $\Lambda > 0$. Thus, stationary bright (dark) solitons can be found with $S < 0$ ($S > 0$). Besides, moving solitons can also exist, featuring a finite group velocity ($v > 0$) that can be found for $k \neq 0$ (Case I) and $k \neq k_{\min}$ (Case II). Returning to original variables, bright soliton solutions (for $\Lambda S < 0$) are given by

$$\begin{pmatrix}\psi_{\uparrow,j}\\ \psi_{\downarrow,j}\end{pmatrix} \approx \begin{pmatrix}1\\ Q\end{pmatrix}\Theta(\xi, \tau)\, e^{iqj}, \tag{20}$$

where

$$\Theta(\xi, \tau) = \rho\,\mathrm{sech}[(\rho\sqrt{|S/\Lambda|})(\xi - v\tau)]e^{ik\xi - i(\omega_- - \rho^2|S|/2)\tau}, \tag{21}$$

with ρ being a free real parameter characterizing the amplitude (width) of the soliton.

Based on the above analysis, in Case II there exist two degenerate minima at specific values of the momentum k, i.e., $k = \pm k_{\min}$, at which two different nonlinear modes can be developed. In the linear limit, a superposition of these modes is still a solution of the equation with the same energy. It turns out to be possible to find a nonlinear solution as a superposition of the two different nonlinear modes developing from $k = \pm k_{\min}$ as well. Particularly, in the case of $W_1 = W_2$, we can employ the symmetry of Eqs. (16), i.e., $c_{\uparrow,q} = -c^*_{\downarrow,q}$, and obtain the *stripe soliton* solution:

$$\begin{pmatrix}\psi_{\uparrow,j}\\ \psi_{\downarrow,j}\end{pmatrix} \approx C\begin{pmatrix}q_+\cos(k_{\min}\xi) + iq_-\sin(k_{\min}\xi)\\ -q_+\cos(k_{\min}\xi) + iq_-\sin(k_{\min}\xi)\end{pmatrix}\Theta(\xi, \tau)e^{iqj}, \tag{22}$$

where $q_\pm = \tilde{\Omega}^{-1} + Q(k = \pm k_{\min})$, $\Theta(\xi, \tau)$ is given by Eq. (21), and C is a free real parameter. The soliton solution given by (22) is localized in the x direction (i.e., along the condensate array) but extended in the y direction (i.e., across the condensate array). We called such a soliton the *1D continuous soliton* since it has a continuous density distribution in the x direction.

Shown in the upper three panels of Fig. 3 are density distributions, $|\psi_{\uparrow,j}|^2 + |\psi_{\downarrow,j}|^2$, of the 1D continuous soliton as functions of $\xi = x/a_z$. When plotting the figure, the SO coupling $\tilde{k}_L$ is taken to be 0.5 in Fig. 3(a), and 1.5 in Fig. 3(b) and Fig. 3(c); other parameters are chosen as $q = 0$ (lattice momentum), $\tilde{\Omega} = 1$ (Raman coupling), $\chi = 1$ (tunneling coefficient), and $W_1 = W_2 = -0.5$ (atomic interactions). The profiles of solitons in the zero-momentum ($k = 0$ for Case I), finite-momentum ($k = k_{\min}$ for Case II), and stripe ($k = \pm k_{\min}$ for Case II) states are illustrated in Figs. 3(a)–3(c), respectively. The left and right insets in each panel show respectively density distributions of the spin-up and spin-down components, $|\psi_{\uparrow,j}|^2$ and $|\psi_{\downarrow,j}|^2$, as functions of $\xi = x/a_z$ and j (the discrete coordinate along y direction). We see that the zero-momentum soliton is unpolarized, $|\psi_{\uparrow,j}|^2 = |\psi_{\downarrow,j}|^2$ [Fig. 3(a)], the finite-momentum soliton is highly polarized, $|\psi_{\uparrow,j}|^2 \ll |\psi_{\downarrow,j}|^2$ [Fig. 3(b)], and the stripe soliton is nearly unpolarized $|\psi_{\uparrow,j}|^2 \approx |\psi_{\downarrow,j}|^2$ [Fig. 3(c)]. Interestingly, an oscillatory behavior emerges on the two sides of the stripe soliton center ($\xi = 0$) [see Fig. 3(c)]. The physical reason of such an oscillatory behavior is due to the interference of the two wave modes with wave numbers $k = k_{\min}$ and $k = -k_{\min}$.

The results for the formation of different spin polarizations of the soliton described above can be understood as follows. For the zero-momentum soliton, the amplitude parameter $Q = -1$ [for the definition of Q, see (18)], and hence the polarization ration (i.e., the ration between the two spin polarization components) $|\psi_{\uparrow,j}|^2/|\psi_{\downarrow,j}|^2 = 1/Q^2 = 1$, i.e., the zero-momentum soliton is always unpolarized; for the finite-momentum soliton, however, one has $Q = -[\tilde{k}_L^2 + (\tilde{k}_L^4 - \tilde{\Omega}^2)^{1/2}]/\tilde{\Omega}$, and hence the polarization ratio is $|\psi_{\uparrow,j}|^2/|\psi_{\downarrow,j}|^2 = 1/Q^2 = \tilde{\Omega}^2/[\tilde{k}_L^2 + (\tilde{k}_L^4 - \tilde{\Omega}^2)^{1/2}]^2 < 1$ when $1 - \tilde{\Omega}/\tilde{k}_L^2 > 0$. With the parameters given above, the polarization ratio of the soliton in Fig. 3(b) is 0.09. Generally, the spin polarization ratio can be tuned actively through changing the SO coupling parameter $\tilde{k}_L$ and/or the Raman coupling parameter $\tilde{\Omega}$.

B. One-dimensional discrete matter-wave solitons localized in the *y* direction

Different from the situation described in the last section, for a 1D soliton localized in the y direction, the condensate array will play a significant role. To obtain the analytical solution of such a soliton, we relax the supposition of exponential dependence on lattices site j and assume that the solution has the following form:

$$\begin{pmatrix}\psi_{\uparrow,j}(\xi, \tau)\\ \psi_{\downarrow,j}(\xi, \tau)\end{pmatrix} = \begin{pmatrix}d_{\uparrow,j}(\tau)\\ d_{\downarrow,j}(\tau)\end{pmatrix} e^{ik\xi + ik^2\tau}. \tag{23}$$

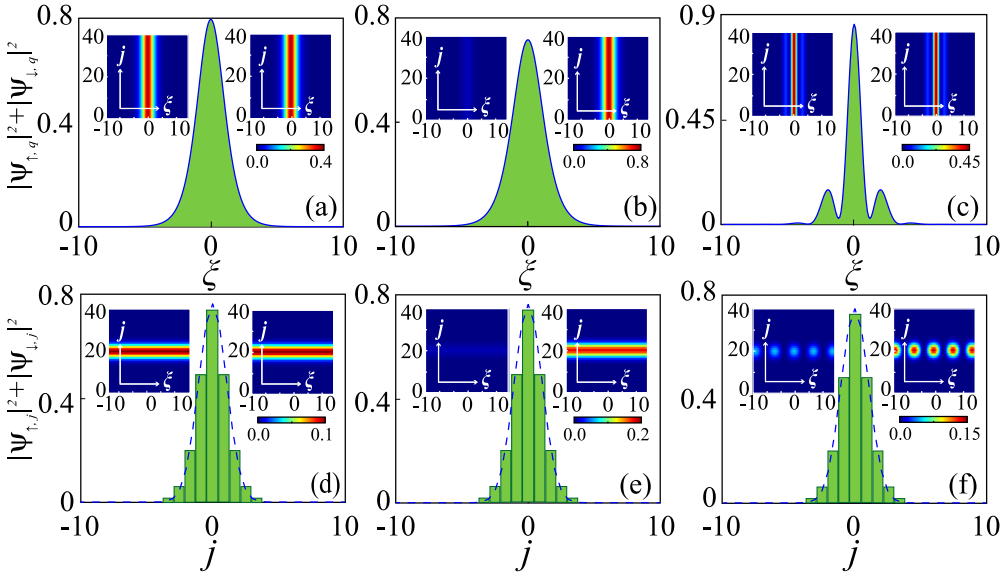

FIG. 3. Density distributions $|\psi_{\uparrow,j}|^2 + |\psi_{\downarrow,j}|^2$ of 1D continuous [panels (a)–(c)] and discrete [panels (d)–(f)] solitons as functions of $\xi = x/a_z$ and j (the discrete coordinate along y direction), respectively. Solitons in the zero-momentum ($k = 0$ for Case I), finite-momentum ($k = k_{\min}$ for Case II), and stripe ($k = \pm k_{\min}$ for Case II) states are respectively shown in the left, middle, and right columns. The left and right inserts in each panel represent density distributions of the spin-up ($|\psi_\uparrow|^2$) and spin-down ($|\psi_\downarrow|^2$) components, respectively. The SO coupling $\tilde{k}_L$ is taken to be 0.5 in the left column, and 1.5 in the middle and right columns. Other parameters are given by $q = 0$ (lattice momentum), $\tilde{\Omega} = 1$ (Raman coupling), $\chi = 1$ (tunneling coefficient), and $W_1 = W_2 = -0.5$ (atomic interactions).

By using Eqs. (11), we obtain the equations for $d_{\uparrow,j}$ and $d_{\downarrow,j}$:

$$i\frac{\partial d_{\uparrow,j}}{\partial \tau} = \tilde{k}_L k\, d_{\uparrow,j} - \chi(d_{\uparrow,j+1} + d_{\uparrow,j-1}) + \tilde{\Omega} d_{\downarrow,j} + (W_1|d_{\uparrow,j}|^2 + W_2|d_{\downarrow,j}|^2)d_{\uparrow,j}, \tag{24a}$$

$$i\frac{\partial d_{\downarrow,j}}{\partial \tau} = -\tilde{k}_L k\, d_{\downarrow,j} - \chi(d_{\downarrow,j+1} + d_{\downarrow,j-1}) + \tilde{\Omega} d_{\uparrow,j} + (W_1|d_{\downarrow,j}|^2 + W_2|d_{\uparrow,j}|^2)d_{\downarrow,j}. \tag{24b}$$

In contrast with Eqs. (16) which are two coupled continuous NLS equations, Eqs. (24) are two coupled discrete NLS equations.

The Lagrangian corresponding to (24) is given by

$$L = \sum_j \left[\sum_{\alpha=\uparrow,\downarrow} \frac{i}{2}(\dot{d}_{\alpha,j} d^*_{\alpha,j} - \dot{d}^*_{\alpha,j} d_{\alpha,j}) - \tilde{G} \right], \tag{25}$$

with

$$\tilde{G} = \tilde{k}_L k(|d_{\uparrow,j}|^2 - |d_{\downarrow,j}|^2) - \chi(d^*_{\uparrow,j} d_{\uparrow,j+1} + d^*_{\downarrow,j} d_{\downarrow,j+1}) + \tilde{\Omega} d^*_{\uparrow,j} d_{\downarrow,j} + \tfrac{1}{2} W_1(|d_{\uparrow,j}|^4 + |d_{\downarrow,j}|^4) + W_2|d_{\uparrow,j}|^2|d_{\downarrow,j}|^2 + \text{c.c.}$$

Here dots stand for time derivative (i.e., ∂_τ) and c.c. stands for complex conjugate. We assume that the width w is much larger than the period of optical lattice $\tilde{d}$, i.e., $w \gg \tilde{d}$, so that the summation over j can be replaced by integration.

Equations (24) can be solved analytically by applying the variational method with the Lagrangian (25) and the following trial function [71,72]:

$$\begin{pmatrix} d_{\uparrow,j} \\ d_{\downarrow,j} \end{pmatrix} = \frac{1}{\sqrt{\sqrt{\pi} 2w}} \begin{pmatrix} e^{i\varphi/2}\sqrt{1+p} \\ -e^{-i\varphi/2}\sqrt{1-p} \end{pmatrix} e^{-\frac{(j-j_c)^2}{2w^2} + iq(j-j_c)}, \tag{26}$$

where p ($-1 < p < 1$), w, j_c, and φ are variation parameters characterizing the spin polarization, width, position, and phase of each spin component, respectively.

The equations of motion for p, w, j_c, and φ can be obtained from the Euler-Lagrangian equation and their steady-state solutions are given as $p = \tilde{k}_L k/(\tilde{k}_L^2 k^2 + \tilde{\Omega}^2)^{1/2} \equiv p_0$, $w = w_0$ (w_0 can be obtained numerically), and $j_c = \varphi = 0$ under the approximation $W_1 \approx W_2$. Then we obtain the soliton solution

$$\begin{pmatrix} \psi_{\uparrow,j} \\ \psi_{\downarrow,j} \end{pmatrix} = \frac{1}{\sqrt{\sqrt{\pi} 2w_0}} \begin{pmatrix} \sqrt{1+p_0} \\ -\sqrt{1-p_0} \end{pmatrix} e^{-\frac{j^2}{2w_0^2} + iqj}\, e^{ik\xi + ik^2\tau}, \tag{27}$$

with the polarization ratio given by $|\psi_{\uparrow,j}|^2/|\psi_{\downarrow,j}|^2 = (1+p_0)/(1-p_0)$. For the zero-momentum ($k = 0$ for Case I) soliton, one has $p_0 = 0$ and hence the polarization ratio $|\psi_{\uparrow,j}|^2/|\psi_{\downarrow,j}|^2 = 1$, i.e., it is always unpolarized. For the finite-momentum ($k = k_{\min}$ for Case II) soliton, one has $p_0 = (1 - \tilde{\Omega}^2/\tilde{k}_L^4)^{1/2}$, and hence the polarization ratio $|\psi_{\uparrow,j}|^2/|\psi_{\downarrow,j}|^2 = [1 - (1 - \tilde{\Omega}^2/\tilde{k}_L^4)^{1/2}]/[1 + (1 - \tilde{\Omega}^2/\tilde{k}_L^4)^{1/2}] < 1$ when $1 - \tilde{\Omega}/\tilde{k}_L^2 > 0$. The soliton solution given by (27) is localized in the y direction (i.e., (across the condensate array) but extended in the x direction (i.e., along the condensate array). We called such a soliton the *1D discrete soliton* since it has a discrete density distribution in the y direction (denoted by the discrete index j).

Shown in the lower part of Fig. 3 are density distributions, $|\psi_{\uparrow,j}|^2 + |\psi_{\downarrow,j}|^2$, of 1D discrete solitons as functions of

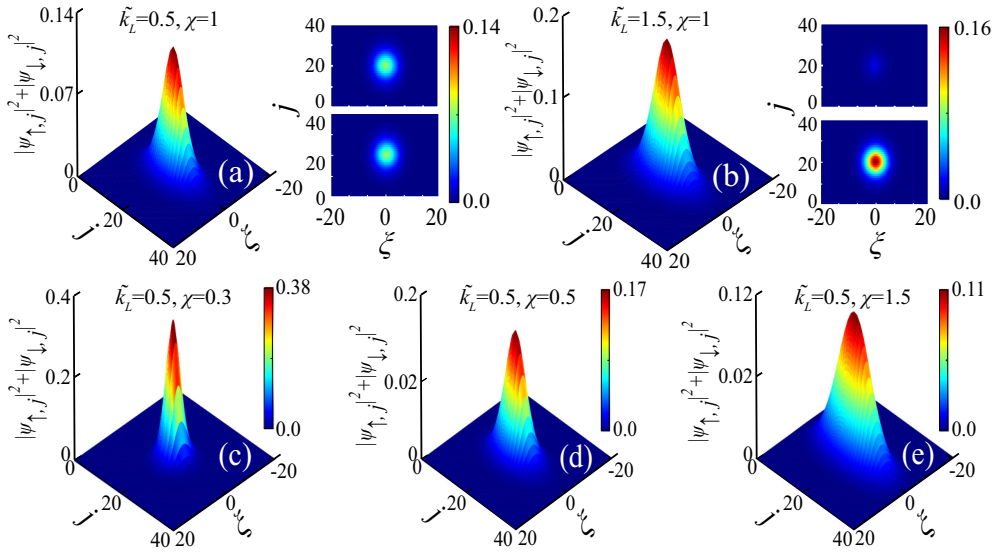

FIG. 4. Density distributions, $|\psi_{\uparrow,j}|^2 + |\psi_{\downarrow,j}|^2$, of the 2D single-peaked semidiscrete solitons as functions of $\xi = x/a_z$ and j with different SO coupling $\tilde{k}_L$ and tunneling coefficient χ. System parameters used are $(\tilde{k}_L, \chi) = (0.5, 1)$ and (1.5,1) for panels (a) and (b), respectively; $(\tilde{k}_L, \chi) = (0.5, 0.3)$, (0.5,0.5), and (0.5,1.5) for panels (c)–(e), respectively. Additionally, in panels (a)–(e), the atomic momentum is $k = 0$, while in panel (b) the atomic momentum is $k = k_{\min}$. Other parameters are given by $q = 0$ (lattice momentum), $\tilde{\Omega} = 1$ (Raman coupling), and $W_1 = W_2 = -0.5$ (atomic interactions). Upper and lower insets in panels (a) and (b) represent density distributions of the spin-up ($|\psi_\uparrow|^2$) and spin-down ($|\psi_\downarrow|^2$) components, respectively.

the lattice site j along the y direction. When plotting the figure, the total number of lattice sites have been chosen to be $J = 40$, the SO coupling $\tilde{k}_L$ is taken as 0.5 in Fig. 3(d) and 1.5 in Figs. 3(e) and 3(f), with other parameters being the same as those used in Figs. 3(a)–3(c). The zero-momentum, finite-momentum, and stripe solitons are illustrated in Figs. 3(d)–3(f), respectively. One sees that there is a spatial modulation of the density distribution in the x direction can be observed for the stripe soliton [see Fig. 3(f)] due to the interference of two modes with $k = \pm k_{\min}$. Moreover, the zero-momentum, finite-momentum, and stripe solitons are unpolarized [i.e., $|\psi_{\uparrow,j}|^2 = |\psi_{\downarrow,j}|^2$; see Fig. 3(d)], highly polarized [i.e., $|\psi_{\uparrow,j}|^2 \ll |\psi_{\downarrow,j}|^2$; see Fig. 3(e)], and partially polarized [i.e., $|\psi_{\uparrow,j}|^2 < |\psi_{\downarrow,j}|^2$; see Fig. 3(f)], respectively.

IV. TWO-DIMENSIONAL SEMIDISCRETE MATTER-WAVE SOLITONS AND THEIR STABILITY

The formation of stable high-dimensional solitons is a more challenging task than those in 1D. The reason is that the cubic nonlinearity usually cannot balance the dispersion (and/or diffraction), resulting in instability (collapse) of solitons in high-dimensional geometries [73]. To arrest the instability, many mechanisms have been proposed, including the employment of trapping potentials and modified nonlinearities of different forms (such as saturable nonlinearity, nonlocal nonlinearity, and so on) [74,75]. Here, we show that, besides the 1D continuous and discrete solitons described in the last section, the system supports also 2D bright matter-wave solitons localized in both x and y directions, which can be stabilized by the combined effects of the atomic dispersion, cubic nonlinearity, SO couplings, and 1D trapping potential in the present system.

Because it is not available to solve Eqs. (11) analytically, we search for the 2D soliton solutions of the system numerically by using the initial condition

$$\begin{pmatrix}\psi_{\uparrow,j}\\ \psi_{\downarrow,j}\end{pmatrix} = \frac{1}{\sqrt{\pi}2R}\begin{pmatrix}\sqrt{1+p}\\ -\sqrt{1-p}\end{pmatrix}\xi^m j^n e^{-\frac{\xi^2+j^2}{2R^2}}, \tag{28}$$

where p is a parameter describing spin polarization, R is the radius of matter-wave beam, and m, n are positive integers (m, $n = 0, 1, 2, \ldots$). The special case $m = n = 0$ describes a 2D soliton with a single-peaked density distribution; cases $m \neq 0$ or $n \neq 0$ describe 2D solitons with density distributions of multiple peaks.

Shown in Fig. 4 are results of numerical simulation for density distributions, $|\psi_{\uparrow,j}|^2 + |\psi_{\downarrow,j}|^2$, of 2D single-peaked solitons as functions of $\xi = x/a_z$ and j with different SO coupling $\tilde{k}_L$ and tunneling coefficient χ. The initial condition is given by (28) with $p = 0$, $R = \sqrt{5}$, and $m = n = 0$. System parameters used are $(\tilde{k}_L, \chi) = (0.5, 1)$ and (1.5,1) for Figs. 4(a) and 4(b), respectively; $(\tilde{k}_L, \chi) = (0.5, 0.3)$, (0.5,0.5), and (0.5,1.5) for Figs. 4(c)–4(e), respectively. Additionally, in Figs. 4(a)–4(e), the atomic momentum k is chosen to be zero (i.e., $k = 0$), while in the Fig. 4(b) the atomic momentum is $k = k_{\min}$. Other parameters are given by $q = 0$ (lattice momentum), $\tilde{\Omega} = 1$ (Raman coupling), and $W_1 = W_2 = -0.5$ (atomic interactions). The upper and lower insets in Figs. 4(a) and 4(b) represent density distributions of the spin-up ($|\psi_\uparrow|^2$) and spin-down ($|\psi_\downarrow|^2$) components, respectively.

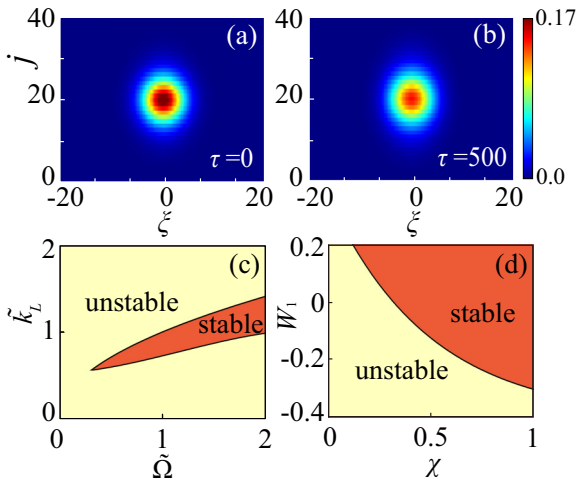

FIG. 5. The stability of single-peaked 2D semidiscrete solitons. (a), (b) Density distributions, $|\psi_{\uparrow,j}|^2 + |\psi_{\downarrow,j}|^2$, of a 2D single-peaked semidiscrete soliton as functions of $\xi = x/a_z$ and j at $\tau = t\omega_z = 0$ and 500, respectively. System parameters used are the same as those in Fig. 4(a). (c), (d) Stability diagrams of 2D single-peaked semidiscrete solitons in parameter spaces of $(\tilde{\Omega}, \tilde{k}_L)$ and (χ, W_1) respectively, with the other system parameters the same as those used in Fig. 4(a).

From the results illustrated in Fig. 4, we see that, similar to the 1D solitons obtained in the last section, the 2D semidiscrete soliton with zero-momentum (i.e., $k = 0$ for Case I) is unpolarized [i.e., $|\psi_{\uparrow,j}|^2 = |\psi_{\downarrow,j}|^2$; see Fig. 4(a)], whereas the 2D semidiscrete soliton with finite-momentum ($k = k_{\min}$ for Case II) is highly polarized [i.e., $|\psi_{\uparrow,j}|^2 \ll |\psi_{\downarrow,j}|^2$; see Fig. 4(b)]. Additionally, when χ is increased but keeping the value of $\tilde{k}_L$, the density maximum of the solitons reduces and its width in the y direction grows [see Figs. 4(c)–4(e)]. The latter phenomenon occurs because larger χ implies stronger tunneling effect between adjacent lattice sites, which leads to a stronger atomic diffusion across the condensate array in the y direction. The variation of χ, however, has a marginal effect on the soliton width in the x direction. Since the solitons obtained above have a continuous density distribution in the x direction but a discrete one in the y direction, we called them *semidiscrete solitons*. Note that 2D semidiscrete solitons were also discovered in other settings, including arrayed or stacked waveguides [76,77], and BECs loaded in an array of one-dimensional trap with Lee-Hung-Yang correction [78].

Importantly, there is a critical value of χ, χ_c, when $\chi > \chi_c$ the 2D semidiscrete solitons shown in Fig. 4 can no longer exist and they will transform into 1D ones. In this case, these 1D solitons are localized only in the continuous direction (x direction) but are delocalized in the discrete direction (y direction), indicating that the atoms have diffused to all lattice sites due to the strong atomic diffusion. By using the parameters provided in Fig. 4, we obtain that $\chi_c \approx 1.7$.

The stability of 2D semidiscrete solitons is checked by evolving Eqs. (11) with small perturbations added to the initial condition, i.e., multiplying the initial condition by the factor $(1 + \epsilon f_R)$, with f_R a random variable uniformly distributed in the interval [0, 1] and ϵ a small parameter. Shown in Figs. 5(a) and 5(b) are density distributions, $|\psi_{\uparrow,j}|^2 + |\psi_{\downarrow,j}|^2$, of a 2D single-peaked semidiscrete soliton as functions of $\xi = x/a_z$ and j at $\tau = t\omega_z = 0$ and the evolution result at $\tau = 500$ (corresponding to $t = 500/\Omega_z \approx 5.3$ s), respectively. The parameters are the same as those used in Fig. 4(a). We see that the soliton is quite stable since it suffers no obvious distortion during propagation.

To study the stability of the 2D semidiscrete solitons in a general way, the soliton fidelity in different parameter spaces are also estimated. The soliton can be taken as stable during propagation if its fidelity exceeds 95% over the evolution time $\tau \leqslant \tau_{\max} = 100$ (corresponding to $t \leqslant 100/\omega_z \approx 1$ s with $\omega_z = 2\pi \times 15$ Hz). Here, the fidelity is defined by [74,79]

$$\mathcal{J} = \left| \sum_j \int [\psi^*_{\uparrow,j}(\tau = 0)\psi_{\uparrow,j}(\tau = \tau_{\max}) + \psi^*_{\downarrow,j}(\tau = 0)\psi_{\downarrow,j}(\tau = \tau_{\max})] d\tau \right|^2 \Big/ (\mathcal{I}_1 \mathcal{I}_2), \quad (29)$$

where

$$\mathcal{I}_1 = \sum_j \int [|\psi_{\uparrow,j}(\tau = 0)|^2 + |\psi_{\downarrow,j}(\tau = 0)|^2] d\xi,$$

$$\mathcal{I}_2 = \sum_j \int [|\psi_{\uparrow,j}(\tau = \tau_{\max})|^2 + |\psi_{\downarrow,j}(\tau = \tau_{\max})|^2] d\xi.$$

It is easily seen that $\mathcal{J} = 1$ at $\tau = 0$ and $0 < \mathcal{J} < 1$ for $0 < \tau < \tau_{\max}$. If $\mathcal{J} \approx 1$, the soliton keeps nearly invariant and hence has a high fidelity; however, if $\mathcal{J} \ll 1$, the soliton suffers a serious distortion and hence is rather unstable during propagation.

Shown in Figs. 5(c) and 5(d) are stability diagrams of 2D single-peaked semidiscrete solitons in parameter spaces $(\tilde{\Omega}, \tilde{k}_L)$ and (χ, W_1), with other parameters being the same as those used in Fig. 4(a); from Fig. 5(c), we see that the semidiscrete solitons are stable when $\tilde{\Omega} \gtrsim 0.3$ and $\tilde{k}_L \approx 1$. From Fig. 5(d), we find that the semidiscrete solitons are stable (unstable) when χ and W_1 are both large (small). A similar result is also obtained for the stability diagram in the parameter space (χ, W_2), where the semidiscrete solitons are stable (unstable) when χ and W_2 are both large (small).

The system can also support 2D semidiscrete solitons with multipeaked density distributions. Shown in Figs. 6(a)–6(c) are $|\psi_{\uparrow,j}|^2 + |\psi_{\downarrow,j}|^2$ of 2D multipeaked semidiscrete solitons as functions of $\xi = x/a_z$ and j for $(\tilde{k}_L, \chi) = (0.5, 0.5)$, $(\tilde{k}_L, \chi) = (0.5, 0.1)$, and $(\tilde{k}_L, \chi) = (0.5, 0.05)$ (i.e., varying χ, fixing $\tilde{k}_L$), respectively. When plotting the figure, other system parameters used are the following: the atomic and lattice momentums $k = q = 0$, the Raman coupling $\tilde{\Omega} = 1$, and the atomic interactions $W_1 = W_2 = -0.2$. Illustrated in the upper inset and lower inset of Fig. 6(a) (where the two peaks are aligned in the x direction) and Fig. 6(b) (where the two peaks are aligned in the y direction) are respectively density distributions of the spin-up and spin-down components (i.e., $|\psi_{\uparrow,j}|^2$ and $|\psi_{\downarrow,j}|^2$), by taking $(m, n) = (1, 0)$ and $(m, n) = (0, 1)$ and the initial conditions given by Figs. 6(a) and 6(b), respectively. These 2D multipeaked semidiscrete solitons are quite stable during evolution due to the joint effects contributed by the

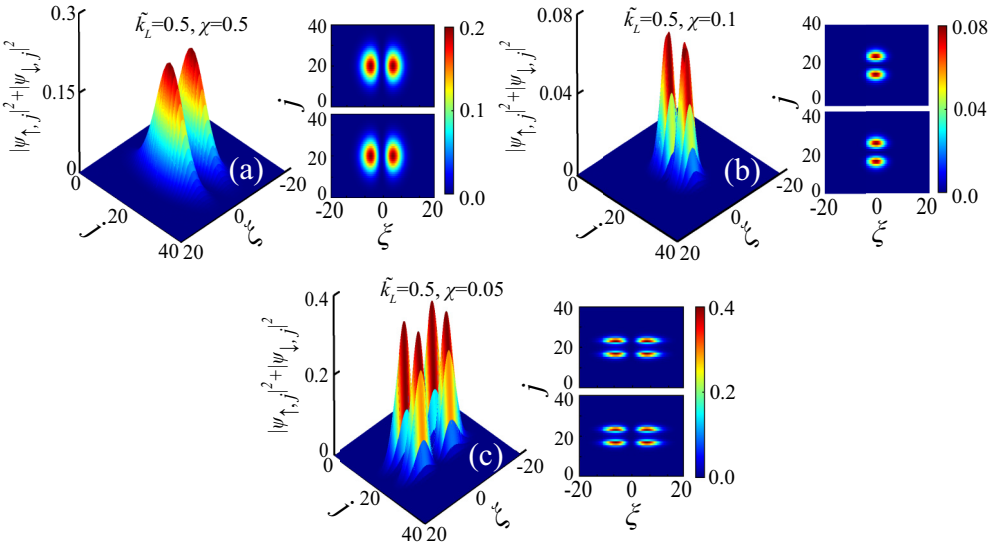

FIG. 6. Density distributions, $|\psi_{\uparrow,j}|^2 + |\psi_{\downarrow,j}|^2$, of 2D multipeaked semidiscrete solitons as functions of $\xi = x/a_z$ and j for $(\tilde{k}_L, \chi) = (0.5, 0.5)$ [panel (a)], $(\tilde{k}_L, \chi) = (0.5, 0.1)$ [panel (b)], and $(\tilde{k}_L, \chi) = (0.5, 0.05)$ [panel (c)]. Two-peaked semidiscrete solitons are observed in the panels (a) and (b), and a four-peaked semidiscrete solitons is observed in panel (c). The upper and lower insets of each panel show respectively density distributions of the spin-up and spin-down components, $|\psi_{\uparrow,j}|^2$ and $|\psi_{\downarrow,j}|^2$. The other system parameters used are atomic and lattice momentums $k = q = 0$, the Raman coupling $\tilde{\Omega} = 1$, and the atomic interactions $W_1 = W_2 = -0.2$.

dispersion, nonlinearity, SO and Raman couplings, and 1D trapping potential in the system.

V. SUMMARY

In this work, we have presented an investigation on the matter-waves solitons in a binary BEC with SO coupling. The BEC is loaded in a 1D deep optical lattice and a 3D anisotropic magnetic trap, by which an array of quasi-1D sub-BECs with transverse tunneling is created. We have shown that the system supports both 1D continuous and discrete solitons, which are localized respectively in the longitudinal (along the array) and the transverse (across the array) directions. We have found that these solitons are unpolarized in zero-momentum state but are polarized in finite-momentum states. Moreover, we have demonstrated that the system supports stable 2D semidiscrete solitons, which can have single-peak and multiple-peaks and are localized in both longitudinal and transverse directions. In addition, we have identified the stability diagrams of the single-peaked semidiscrete solitons in different parameter spaces.

The model suggested in this work can be extended to study other types of high-dimensional nonlinear excitations, e.g., matter-wave vortex solitons and soliton molecules [79], if a nonlocal atom-atom interaction (which can be realized by using dipolar BECs) is taken into account. The results reported here are beneficial for understanding the unique property of SO-coupled BECs and provide a new route for generating novel matter-wave solitons that are stable during propagation based on Bose-condensed atomic gases.

ACKNOWLEDGMENTS

This work is supported by National Natural Science Foundation of China (NSFC) under Grants No. 11974117 and No. 11975098, National Key Research and Development Program of China under Grant No. 2017YFA0304201, and Shanghai Municipal Science and Technology Major Project under Grant No. 2019SHZDZX01.

[1] H. Haken and H. C. Wolf, *The Physics of Atoms and Quanta: Introduction to Experiments and Theory*, 7th ed. (Springer, Berlin, 2005).

[2] X. L. Qi and S. C. Zhang, The quantum spin Hall effect and topological insulators, Phys. Today **63**(1), 33 (2010).

[3] M. Z. Hasan and C. L. Kane, Topological insulators, Rev. Mod. Phys. **82**, 3045 (2010).

[4] Y. K. Kato, R. C. Myers, A. C. Gossard, and D. D. Awschalom, Observation of the spin Hall effect in semiconductors, Science **306**, 1910 (2004).

[5] J. Sinova, S. O. Valenzuela, J. Wunderlich, C. H. Back, and T. Jungwirth, Spin Hall effects, Rev. Mod. Phys. **87**, 1213 (2015).

[6] I. Žutić, J. Fabian, and S. Das Sarma, Spintronics: Fundamentals and applications, Rev. Mod. Phys. **76**, 323 (2004).

[7] J. D. Koralek, C. P. Weber, J. Orenstein, B. A. Bernevig, S. C. Zhang, S. Mack, and D. D. Awschalom, Emergence of the persistent spin helix in semiconductor quantum wells, Nature (London) **458**, 610 (2009).

[8] T. D. Stanescu, B. Anderson, and V. Galitski, Spin-orbit coupled Bose-Einstein condensates, Phys. Rev. A **78**, 023616 (2008).

[9] Y.-J. Lin, R. L. Compton, A. R. Perry, W. D. Phillips, J. V. Porto, and I. B. Spielman, Bose-Einstein Condensate in a Uniform Light-Induced Vector Potential, Phys. Rev. Lett. **102**, 130401 (2009).

[10] Y. J. Lin, K. Jiménez-García, and I. B. Spielman, Spin-orbit-coupled Bose-Einstein condensates, Nature (London) **471**, 83 (2011).

[11] P. J. Wang, Z. Q. Yu, Z. K. Fu, J. Miao, L. H. Huang, S. J. Chai, H. Zhai, and J. Zhang, Spin-Orbit Coupled Degenerate Fermi Gases, Phys. Rev. Lett. **109**, 095301 (2012).

[12] L. W. Cheuk, A. T. Sommer, Z. Hadzibabic, T. Yefsah, W. S. Bakr, and M. W. Zwierlein, Spin-Injection Spectroscopy of a Spin-Orbit Coupled Fermi Gas, Phys. Rev. Lett. **109**, 095302 (2012).

[13] J. Y. Zhang, S. C. Ji, Z. Chen, L. Zhang, Z. D. Du, B. Yan, G. S. Pan, B. Zhao, Y. J. Deng, H. Zhai, S. Chen, and J. W. Pan, Collective Dipole Oscillations of a Spin-Orbit Coupled Bose-Einstein Condensate, Phys. Rev. Lett. **109**, 115301 (2012).

[14] Z. Wu, L. Zhang, W. Sun, X. T. Xu, B. Z. Wang, S. C. Ji, Y. Deng, S. Chen, X. J. Liu, and J. W. Pan, Realization of two-dimensional spin-orbit coupling for Bose-Einstein condensates, Science **354**, 83 (2016).

[15] L. Huang, Z. Meng, P. Wang, P. Peng, S. L. Zhang, L. Chen, D. Li, Q. Zhou, and J. Zhang, Experimental realization of two-dimensional synthetic spin-orbit coupling in ultracold Fermi gases, Nat. Phys. **12**, 540 (2016).

[16] J. Dalibard, F. Gerbier, G. Juzeliūnas, and P. Öhberg, Artificial gauge potentials for neutral atoms, Rev. Mod. Phys. **83**, 1523 (2011).

[17] V. Galitski and I. B. Spielman, Spin-orbit coupling in quantum gases, Nature (London) **494**, 49 (2013).

[18] X. Zhou, Y. Li, Z. Cai, and C. Wu, Unconventional states of bosons with the synthetic spin-orbit coupling, J. Phys. B: At., Mol. Opt. Phys. **46**, 134001 (2013).

[19] N. Goldman, G. Juzeliūnas, P. Öhberg, and I. B. Spielman, Light-induced gauge fields for ultracold atoms, Rep. Prog. Phys. **77**, 126401 (2014).

[20] H. Zhai, Degenerate quantum gases with spin-orbit coupling: A review, Rep. Prog. Phys. **78**, 026001 (2015).

[21] W. Yi, W. Zhang, and X. Cui, Pairing superfluidity in spin-orbit coupled ultracold Fermi gases, Sci. China: Phys., Mech. Astron. **58**, 1 (2015).

[22] J. Zhang, H. Hu, X.-J. Liu, and H. Pu, Fermi gases with synthetic spin-orbit coupling, Annu. Rev. Cold At. Mol. **2**, 81 (2014).

[23] C. Wang, C. Gao, C.-M. Jian, and H. Zhai, Spin-Orbit Coupled Spinor Bose-Einstein Condensates, Phys. Rev. Lett. **105**, 160403 (2010).

[24] T.-L. Ho and S. Zhang, Bose-Einstein Condensates with Spin-Orbit Interaction, Phys. Rev. Lett. **107**, 150403 (2011).

[25] S. Sinha, R. Nath, and L. Santos, Trapped Two-Dimensional Condensates with Synthetic Spin-Orbit Coupling, Phys. Rev. Lett. **107**, 270401 (2011).

[26] Y. Li, L. P. Pitaevskii, and S. Stringari, Quantum Tricriticality and Phase Transitions in Spin-Orbit Coupled Bose-Einstein Condensates, Phys. Rev. Lett. **108**, 225301 (2012).

[27] Y. Li, G. I. Martone, L. P. Pitaevskii, and S. Stringari, Superstripes and the Excitation Spectrum of a Spin-Orbit-Coupled Bose-Einstein Condensate, Phys. Rev. Lett. **110**, 235302 (2013).

[28] Y. Deng, J. Cheng, H. Jing, C.-P. Sun, and S. Yi, Spin-Orbit-Coupled Dipolar Bose-Einstein Condensates, Phys. Rev. Lett. **108**, 125301 (2012).

[29] Y. Zhang, L. Mao, and C. Zhang, Mean-Field Dynamics of Spin-Orbit Coupled Bose-Einstein Condensates, Phys. Rev. Lett. **108**, 035302 (2012).

[30] C. Qu, C. Hamner, M. Gong, C. Zhang, and P. Engels, Observation of Zitterbewegung in a spin-orbit-coupled Bose-Einstein condensate, Phys. Rev. A **88**, 021604(R) (2013).

[31] M. A. Khamehchi, Y. Zhang, C. Hamner, T. Busch, and P. Engels, Measurement of collective excitations in a spin-orbit-coupled Bose-Einstein condensate, Phys. Rev. A **90**, 063624 (2014).

[32] S.-C. Ji, L. Zhang, X.-T. Xu, Z. Wu, Y. Deng, S. Chen, and J.-W. Pan, Softening of Roton and Phonon Modes in a Bose-Einstein Condensate with Spin-Orbit Coupling, Phys. Rev. Lett. **114**, 105301 (2015).

[33] H. Lyu and Y. Zhang, Spin-orbit-coupling-assisted roton softening and superstripes in a Rydberg-dressed Bose-Einstein condensate, Phys. Rev. A **102**, 023327 (2020).

[34] M. Merkl, A. Jacob, F. E. Zimmer, P. Öhberg, and L. Santos, Chiral Confinement in Quasirelativistic Bose-Einstein Condensates, Phys. Rev. Lett. **104**, 073603 (2010).

[35] D. A. Zezyulin, R. Driben, V. V. Konotop, and B. A. Malomed, Nonlinear modes in binary bosonic condensates with pseudo-spin-orbital coupling, Phys. Rev. A **88**, 013607 (2013).

[36] V. Achilleos, D. J. Frantzeskakis, P. G. Kevrekidis, and D. E. Pelinovsky, Matter-Wave Bright Solitons in Spin-Orbit Coupled Bose-Einstein Condensates, Phys. Rev. Lett. **110**, 264101 (2013).

[37] Y. Xu, Y. Zhang, and B. Wu, Bright solitons in spin-orbit coupled Bose-Einstein condensates, Phys. Rev. A **87**, 013614 (2013).

[38] L. Salasnich and B. A. Malomed, Localized modes in dense repulsive and attractive Bose-Einstein condensates with spin-orbit and Rabi couplings, Phys. Rev. A **87**, 063625 (2013).

[39] J. Sun, Y. Chen, X. Chen, and Y. Zhang, Bright solitons in a spin-tensor-momentum-coupled Bose-Einstein condensate, Phys. Rev. A **101**, 053621 (2020).

[40] L. Salasnich, W. B. Cardoso, and B. A. Malomed, Localized modes in quasi-two-dimensional Bose-Einstein condensates with spin-orbit and Rabi couplings, Phys. Rev. A **90**, 033629 (2014).

[41] H. Sakaguchi, B. Li, and B. A. Malomed, Creation of two-dimensional composite solitons in spin-orbit-coupled self-attractive Bose-Einstein condensates in free space, Phys. Rev. E **89**, 032920 (2014).

[42] H. Sakaguchi and B. A. Malomed, Discrete and continuum composite solitons in Bose-Einstein condensates with the Rashba spin-orbit coupling in one and two dimensions, Phys. Rev. E **90**, 062922 (2014).

[43] H. Sakaguchi, E. Ya. Sherman, and B. A. Malomed, Vortex solitons in two-dimensional spin-orbit-coupled Bose-Einstein condensates: Effects of the Rashba-Dresselhaus coupling and Zeeman splitting, Phys. Rev. E **94**, 032202 (2016).

[44] Y. Xu, Y. Zhang, and C. Zhang, Bright solitons in a two-dimensional spin-orbit-coupled dipolar Bose-Einstein condensate, Phys. Rev. A **92**, 013633 (2015).

[45] X. Jiang, Z. Fan, Z. Chen, W. Pang, Y. Li, and B. A. Malomed, Two-dimensional solitons in dipolar Bose-Einstein condensates with spin-orbit coupling, Phys. Rev. A **93**, 023633 (2016).

[46] Y. Li, Y. Liu, Z. Fan, W. Pang, S. Fu, and B. A. Malomed, Two-dimensional dipolar gap solitons in free space with spin-orbit coupling, Phys. Rev. A **95**, 063613 (2017)

[47] S. K. Adhikari, Multiring, stripe, and superlattice solitons in a spin-orbit-coupled spin-1 condensate, Phys. Rev. A **103**, L011301 (2021).

[48] Y.-C. Zhang, Z-W. Zhou, B. A. Malomed, and H. Pu, Stable Solitons in Three Dimensional Free Space without the Ground State: Self-Trapped Bose-Einstein Condensates with Spin-Orbit Coupling, Phys. Rev. Lett. **115**, 253902 (2015).

[49] O. Fialko, J. Brand, and U. Zülicke, Soliton magnetization dynamics in spin-orbit-coupled Bose-Einstein condensates, Phys. Rev. A **85**, 051605(R) (2012).

[50] V. Achilleos, J. Stockhofe, P. G. Kevrekidis, D. J. Frantzeskakis, and P. Schmelcher, Matter-wave dark solitons and their excitation spectra in spin-orbit coupled Bose-Einstein condensates, Europhys. Lett. **103**, 20002 (2013).

[51] Y. Xu, L. Mao, B. Wu, and C. Zhang, Dark Solitons with Majorana Fermions in Spin-Orbit-Coupled Fermi Gases, Phys. Rev. Lett. **113**, 130404 (2014).

[52] P. Zou, J. Brand, X.-J. Liu, and H. Hu, Traveling Majorana Solitons in a Low-Dimensional Spin-Orbit-Coupled Fermi Superfluid, Phys. Rev. Lett. **117**, 225302 (2016).

[53] A. Muñoz Mateo and X. Yu, Two types of dark solitons in a spin-orbit-coupled Fermi gas, Phys. Rev. A **105**, L021301 (2022).

[54] L.-C. Zhao, X-W. Luo, and C. Zhang, Magnetic stripe soliton and localized stripe wave in spin-1 Bose-Einstein condensates, Phys. Rev. A **101**, 023621 (2020).

[55] Y. V. Kartashov, V. V. Konotop, and F. K. Abdullaev, Gap Solitons in a Spin-Orbit-Coupled Bose-Einstein Condensate, Phys. Rev. Lett. **111**, 060402 (2013).

[56] V. E. Lobanov, Y. V. Kartashov, and V. V. Konotop, Fundamental, Multipole, and Half-Vortex Gap Solitons in Spin-Orbit Coupled Bose-Einstein Condensates, Phys. Rev. Lett. **112**, 180403 (2014).

[57] Y. Zhang, Y. Xu, and T. Busch, Gap solitons in spin-orbit-coupled Bose-Einstein condensates in optical lattices, Phys. Rev. A **91**, 043629 (2015).

[58] X. Zhu, H. Li, Z. Shi, Y. Xiang and Y. He, Gap solitons in spin-orbit-coupled Bose-Einstein condensates in mixed linear-nonlinear optical lattices, J. Phys. B: At., Mol. Opt. Phys. **50**, 155004 (2017).

[59] Y. V. Kartashov and D. A. Zezyulin, Stable Multiring and Rotating Solitons in Two-Dimensional Spin-Orbit-Coupled Bose-Einstein Condensates with a Radially Periodic Potential, Phys. Rev. Lett. **122**, 123201 (2019).

[60] Q. Zhu, C. Zhang, and B. Wu, Exotic superfluidity in spin-orbit coupled Bose-Einstein condensates, Europhys. Lett. **100**, 50003 (2012).

[61] C. Hamner, Y. Zhang, M. A. Khamehchi, M. J. Davis, and P. Engels, Spin-Orbit-Coupled Bose-Einstein Condensates in a One-Dimensional Optical Lattice, Phys. Rev. Lett. **114**, 070401 (2015).

[62] M. Salerno and F. K. Abdullaev, Symmetry breaking of localized discrete matter waves induced by spin-orbit coupling, Phys. Lett. A **379**, 2252 (2015).

[63] M. Salerno, F. K. Abdullaev, A. Gammal, and L. Tomio, Tunable spin-orbit-coupled Bose-Einstein condensates in deep optical lattices, Phys. Rev. A **94**, 043602 (2016).

[64] M. Johansson, P. P. Beličev, G. Gligorič, D. R. Gulevich, and D. V. Skryabin, Nonlinear gap modes and compactons in a lattice model for spin-orbit coupled exciton-polaritons in zigzag chains, J. Phys. Commun. **3**, 015001 (2019).

[65] P. P. Beličev, G. Gligorić, J. Petrovic, A. Maluckov, L. Hadžievski, and B. A Malomed, Composite localized modes in discretized spin-orbit-oupled Bose-Einstein condensates, J. Phys. B: At., Mol. Opt. Phys. **48**, 065301 (2015).

[66] S. L. Cornish, S. T. Thompson, and C. E. Wieman, Formation of Bright Matter-Wave Solitons during the Collapse of Attractive Bose-Einstein Condensates, Phys. Rev. Lett. **96**, 170401 (2006).

[67] A. L. Marchant, T. P. Billam, T. P. Wiles, M. M. H. Yu, S. A. Gardiner, and S. L. Cornish, Controlled formation and reflection of a bright solitary matter-wave, Nat. Commun. **4**, 1865 (2013).

[68] C. Kittel, *Introduction to the Solid State Theory* (Cambridge University Press, Cambridge, 1975).

[69] G. L. Alfimov, P. G. Kevrekidis, V. V. Konotop, and M. Salerno, Wannier functions analysis of the nonlinear Schrödinger equation with a periodic potential, Phys. Rev. E **66**, 046608 (2002).

[70] J. J. Sakurai, *Modern Quantum Mechanics (Revised Edition)* (Addison Wesley, New York, 1993).

[71] Z. F. Yu, A. X. Zhang, R. A. Tang, H. P. Xu, J. M. Gao, and J. K. Xue, Spin-orbit-coupling stabilization of a collapsing binary Bose-Einstein condensate, Phys. Rev. A **95**, 033607 (2017).

[72] Y. C. Zhang, Y. Jian, Z. F. Yu, A. X. Zhang, and J. K. Xue, Stability and quantum escape dynamics of spin-orbit-coupled Bose-Einstein condensates in the shallow trap, Phys. Rev. E **102**, 032220 (2020).

[73] L. Bergé, Wave collapse in physics: Principles and applications to light and plasma waves, Phys. Rep. **303**, 259 (1998).

[74] Z. Bai, W. Li, and G. Huang, Stable single light bullets and vortices and their active control in cold Rydberg gases, Optica **6**, 309 (2019).

[75] B. A. Malomed, *Multidimensional Solitons* (AIP Publishing, Melville, 2022).

[76] N.-C. Panoiu, B. A. Malomed, and R. M. Osgood Jr., Semidiscrete solitons in arrayed waveguide structures with Kerr nonlinearity, Phys. Rev. A **78**, 013801 (2008).

[77] R. Blit and B. A. Malomed, Propagation and collisions of semidiscrete solitons in arrayed and stacked waveguides, Phys. Rev. A **86**, 043841 (2012).

[78] X. Zhang, X. Xu, Y. Zheng, Z. Chen, B. Liu, C. Huang, B. A. Malomed, and Y. Li, Semidiscrete Quantum Droplets and Vortices, Phys. Rev. Lett. **123**, 133901 (2019).

[79] L. Qin, C. Hang, B. A. Malomed, G. Huang, Stable high-dimensional weak-light soliton molecules and their active control, Laser Photonics Rev. **16**, 2100297 (2022).